applied sciences

MDPI

Article

Influence of Solution Treatment Temperatures on LPBF-Produced Inconel 939 Alloy on Mechanical Performance

Piotr Piwowarski, Dorota Moszczyńska *, Krystian Paradowski, Monika Wieczorek-Czarnocka and Jarosław Mizera

Faculty of Materials Science and Engineering, Warsaw University of Technology, 00-645 Warsaw, Poland; piotr.piwowarski3.dokt@pw.edu.pl (P.P.); krystian.paradowski@pw.edu.pl (K.P.); monika.wieczorek-czarnocka@pw.edu.pl (M.W.-C.); jaroslaw.mizera@pw.edu.pl (J.M.)
* Correspondence: dorota.moszczynska@pw.edu.pl

Abstract: This study investigates the influence of solution treatment temperatures on the microstructure and mechanical properties of LPBF (Laser Powder Bed Fusion)-manufactured Inconel 939 alloy. The primary objectives are to assess the impact of sub-recrystallization (below recrystallization temperature) and recrystallization temperatures during solution treatment on mechanical performance under different conditions. This study validates the hypothesis concerning carbide redistribution and mechanical performance in LPBF-produced Inconel 939 parts through comprehensive analysis, including microstructure studies and tensile tests. The results indicate that higher heat treatment temperatures lead to significant changes in carbide redistribution and mechanical performance. For instance, at room temperature, the specimen with sub-recrystallization solution treatment temperature exhibited superior mechanical properties compared to both the as-built and recrystallization-temperature solution treatment specimens. However, at elevated temperatures (700 °C), a reversal in mechanical anisotropy was observed, with the vertical axis demonstrating higher tensile strength compared to the horizontal axis for all material states. Furthermore, a microstructural analysis revealed distinct changes in grain structure and precipitate distribution, particularly the migration of carbides from grain boundaries to intragranular regions. These findings underscore the importance of precise control over heat treatment parameters to achieve optimal mechanical behavior. This research provides valuable insights into optimizing LPBF processes for the Inconel 939 alloy, highlighting the need for a meticulous control of the solution treatment parameters to ensure mechanical integrity. The findings contribute to a broader understanding of material-specific responses in additive manufacturing, with significant implications for aerospace applications.

Keywords: Inconel 939; additive manufacturing; heat treatment; mechanical properties

check for updates

Citation: Piwowarski, P.; Moszczyńska, D.; Paradowski, K.; Wieczorek-Czarnocka, M.; Mizera, J. Influence of Solution Treatment Temperatures on LPBF-Produced Inconel 939 Alloy on Mechanical Performance. *Appl. Sci.* **2024**, *14*, 9625. https://doi.org/10.3390/app14219625

Academic Editor: John D. Clayton

Received: 17 September 2024
Revised: 8 October 2024
Accepted: 17 October 2024
Published: 22 October 2024

Copyright: © 2024 by the authors. Licensee MDPI, Basel, Switzerland. This article is an open access article distributed under the terms and conditions of the Creative Commons Attribution (CC BY) license (https://creativecommons.org/licenses/by/4.0/).

1. Introduction

In aerospace engineering, the pursuit of more efficient propulsion systems remains a top priority [1]. This drive necessitates the exploration of advanced materials and manufacturing techniques [2] capable of enduring extreme conditions while delivering optimal performance. LPBF has transformed manufacturing by enabling the precise fabrication of intricate geometries using metallic powders. Notably, this technique is vital for creating rocket nozzles with internal cooling channels, which is crucial for enduring extreme temperatures and pressures during propulsion.

However, while LPBF holds immense promise for aerospace engineering, it also poses challenges. Thermal gradients and rapid solidification rates during laser melting can result in non-equilibrium microstructures, impacting material properties. Residual stresses and porosity inherent in the layer-by-layer build strategy of LPBF can affect mechanical behavior and long-term performance. Consequently, meticulous control over process parameters is

essential to ensure consistent part quality, emphasizing the need for comprehensive process monitoring and optimization techniques [3–5].

Nickel-based superalloys have emerged as key candidates, offering exceptional mechanical properties and high-temperature resistance. Inconel 939, in particular, has attracted attention due to its impressive blend of strength, corrosion resistance, and thermal stability at elevated temperatures.

Additive manufacturing methods, especially Laser Powder Bed Fusion (LPBF), coupled with innovative heat treatment approaches, offer promising avenues for maximizing Inconel 939's potential in aerospace applications.

The integration of Inconel 939 into the LPBF process presents an opportunity to address LPBF challenges and unlock new possibilities in aerospace component production. To fully exploit this potential, understanding and optimizing heat treatment protocols tailored to LPBF-produced Inconel 939 components are imperative. Standard heat treatment typically involves solution treatment and aging steps aimed at homogenizing the microstructure and enhancing mechanical properties. Solution treatment dissolves γ' created during the LPBF process, facilitating a supersaturated solid solution. It also removes deleterious η phase, which was confirmed in Inconel 939 by Shaikh et al. (2023) [6]. Different aging parameters focus on the growth of specific phases, thus resulting in differences between research papers. The most common aging steps are within the range of γ' phase growth, as it is the primary strengthening mechanism of this alloy.

Shaikh (2018) [7] reported the upper range of the solidus phase temperature at 1250 °C ± 30, higher than the reported 1235 °C provided by Gibbons et al. [8] and Formenti et al. [9]. Banoth et al. [10] highlighted the impact of solution treatment temperatures, particularly recrystallization temperature, on creep properties. They argued that a 1240 °C solution treatment effectively eliminates residual stresses and improves grain size, enhancing creep life. This treatment doubled the average grain size and significantly increased the recrystallization factor (66% vs. 12.8%), resulting in nearly three times longer creep life compared to the sub-recrystallization treatments. Consequently, 1210 °C was chosen for sub-recrystallization and 1240 °C for the recrystallization solution treatments. For the aging process, EOS standard heat treatment [11] steps II and III are optimal: at 1000 °C, initial γ' phase growth with limited η phase growth occurs, and at 800 °C, further γ' phase growth without η phase growth is observed.

The aim of this study is to investigate the influence of sub-recrystallization and recrystallization temperatures during solution treatment on mechanical properties. By analyzing carbide redistribution and morphological changes in grains and subgrains, this study seeks to optimize the heat treatment parameters to achieve the optimal mechanical properties of LPBF-produced Inconel 939.

The research hypothesis suggests that increasing the solution treatment temperature will have an impact on carbide redistribution, thereby improving the mechanical performance of LPBF-produced Inconel 939. Through a series of research questions, this study aims to clarify the prerequisites for achieving carbide redistribution, evaluate the influence of heat treatment parameters on the microstructure, and assess the effects of grain size on mechanical behavior.

2. Methodology

2.1. Specimen Manufacturing

The Inconel 939 powder was purchased from EOS GmbH (Krailling, Germany), with declared chemical composition (wt%) as in Table 1. Powder size distribution was investigated using anLA-950 laser diffraction powder analyzer (Horiba, Ltd., Kyoto, Japan) with a measured diameter (10–90%) between 18 and 49 μm with a median of 29 μm. The shape of the particles was analyzed using a TM-1000 SEM (Hitachi, Ltd., Tokyo, Japan) microscope. Particles were mostly round with visible dendrites on the surface (Figure 1).

Table 1. Inconel 939 declared chemical composition (wt%).

Ni	Cr	Co	W	Nb	Ti	Al	Ta	Zr	C	B
48.24	22.5	19.0	2.0	1.0	3.7	1.9	1.4	0.1	0.15	0.01

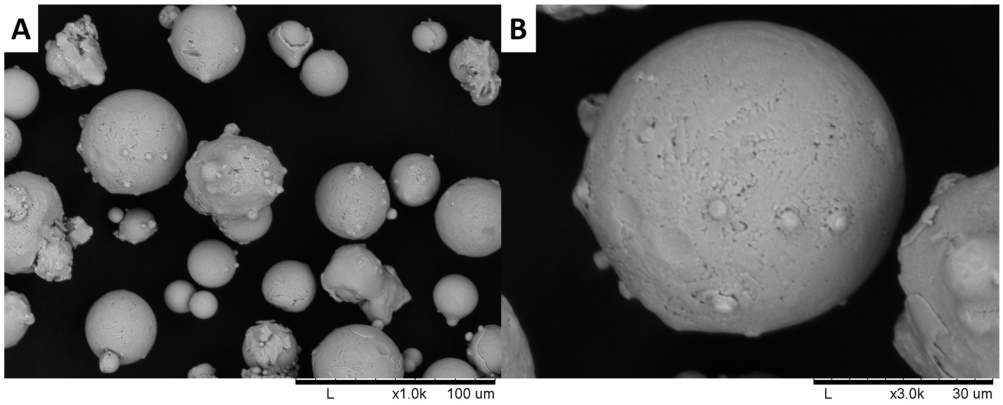


Figure 1. SEM micrographs of Inconel 939 powder particles at ×1000 magnification (**A**) and ×3000 magnification (**B**).

Specimens were prepared using an EOS M100 (EOS GmbH, Krailling, Germany) machine equipped with a 200 W Yb fiber laser. Cube specimens 8 × 8 × 8 mm were produced to optimize process parameters using hardness and porosity analysis. The optimized parameters were laser power, hatching distance, and scanning speed. Following the statistical analysis of the optimization results, the following process parameters were chosen: laser power of 117 W, scanning speed of 1000 mm/s, and hatching distance of 0.05 mm. Specimens for tensile tests were cut from bulk 20 × 15 × 18 mm cuboid parts.

2.2. Heat Treatment

Specimens were heat treated according to Table 2. Both heat treatments are a modification of the standard heat treatment for LPBF-printed Inconel 939 provided by EOS [11] with different solution treatment parameters (1st step). HT1 state has a solution treatment temperature of 1210 °C (sub-recrystallization temperature). HT2 state has a solution treatment temperature of 1240 °C (recrystallization temperature). The furnace had a non-inert atmosphere.

Table 2. Heat treatment parameters.

	Step 1	Cooling	Step 2	Cooling	Step 3	Cooling
HT1	1210/8 h	FAC	1000/6 h	FAC	800/4 h	AC
HT2	1240/8 h	FAC	1000/6 h	FAC	800/4 h	AC

2.3. Two-Dimensional Porosity Analysis

Specimens for porosity analysis were cut in half to expose the XZ and XY planes, included in thermal conductive resin, and polished (320, 640, 1280 grade papers, 3 µm, 1 µm diamond solution). In total, 12 micrographs at ×50 magnification were made for each set of parameters, both in the XZ and XY planes. Images were then converted to binary images at specific thresholds, and the number of black pixels (representing pores) was subsequently counted to determine the porosity percentage. The exhibited density for the chosen parameter set was 99.99% using the described methodology.

2.4. Microstructure Observations

Microstructure observations were conducted using optical microscopy and scanning electron microscopy (SEM) with EDS and EBSD detectors. For optical microscopy observations, Carl ZEISS Axio Scope.A1 was used, while for high magnification observations, Hitachi SU70 was used. Specimen preparation was the same as for the porosity analysis, with additional etching using Kalling's No. 2 solution for optical microscopy and SEM.

2.5. Hardness Tests

Hardness tests were conducted using the Zwick/Roell ZHV30 (Zwick GmbH, Ulm, Germany) hardness tester with a Vickers indenter with a 98.07 N (HV10) load. Specimens were prepared in the same way as for the porosity analysis. Each specimen was measured in the XZ and XY planes, with 5 measurements taken from the edge of the specimen towards the center (Figure 2C).

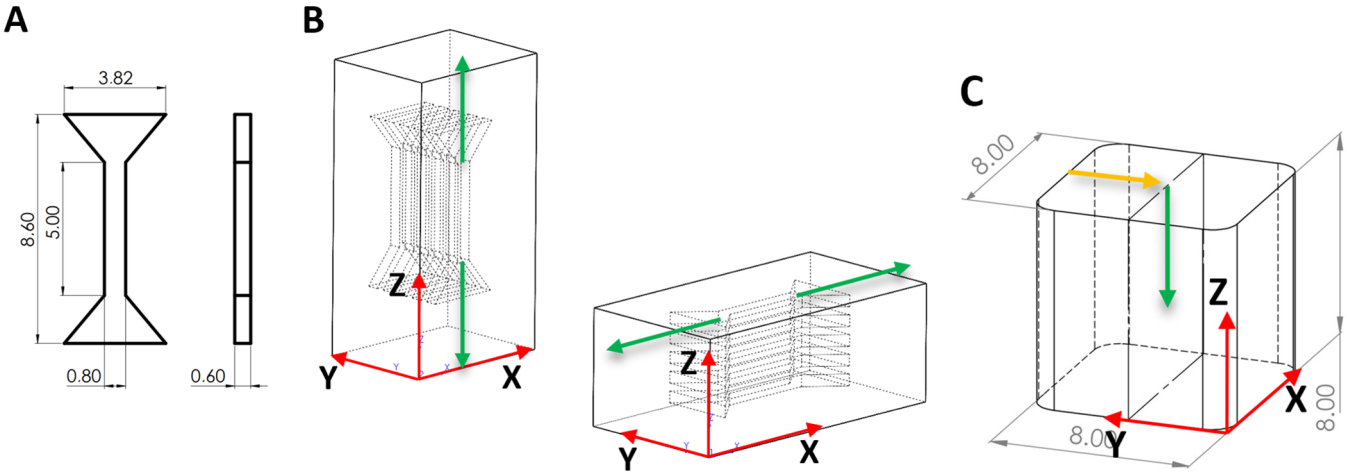


Figure 2. Specimens for tensile and hardness tests. The red arrows indicate the axis direction. Dimensions of the tensile specimen (**A**). Placement of the tensile mini specimens inside the bulk cuboids—the green arrows indicate the direction of the tensile force (**B**). Cube specimen for porosity analysis, hardness tests, and microstructure observations—the gold arrow indicates the direction of the hardness tests in the XY plane, and the green arrow indicates the direction of the hardness tests in the XZ plane (**C**).

2.6. Tensile Tests

Specimens used for tensile tests performed at room temperature (23 °C) and elevated temperature (700 °C) were mini tensile specimens cut out from bulk specimens using WEDM (Figure 2A,B) (Molak et al. [12,13]). Tensile tests were performed on normal and modified Zwick/Roell Z050 universal testing machines with tensile setup for mini specimens. Modifications for elevated temperature tensile tests included a custom specimen mount from Rene 41 alloy and an electrical furnace installed around the specimen mount. Specimens for elevated temperature tests were heated to the final temperature and held at it for 10 min before the tensile tests were performed. At least four specimens were tested for each material state and axis to ensure comprehensive mechanical property characterization. Ultimate tensile strength (UTS/Rm) and yield strength (R0.2) were measured.

3. Results and Discussion

3.1. Mechanical Testing

3.1.1. Hardness Tests

After the heat treatments, both specimens exhibited 33% higher hardness compared to the as-built state. The hardness difference between the HT1 and HT2 states was minimal (0.5%). A change in anisotropy was observed, with differences between testing directions

decreasing from 4.6% (AB) to 0.5% (HT1) and 1.6% (HT2) (Figure 3). Compared to the powder manufacturer's data, the as-built state exhibited a 2.4% higher hardness (compared to 33 HRC). The heat-treated states exhibited a 6.9% (HT1) and 7.4% (HT2) lower hardness compared to the manufacturer's data (48 HRC for the heat-treated state).

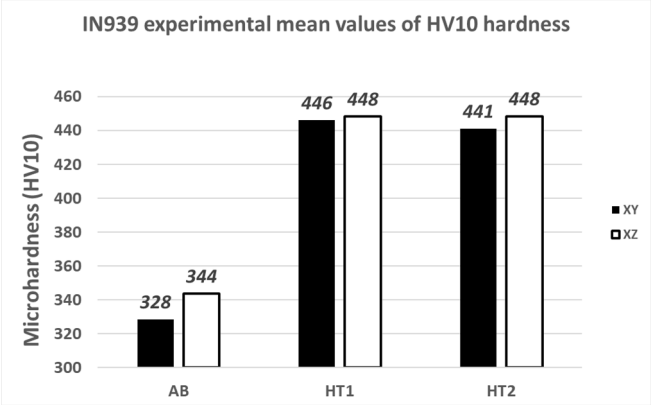


Figure 3. Inconel 939 hardness for as-built, HT1, and HT2 states.

3.1.2. Tensile Tests

At room temperature, the tensile properties of the as-built specimens were comparable to the manufacturer's reference as-built state [11], with the exception of a UTS in the vertical (Z-axis) direction (which had a 9% lower value). The HT1 state exhibited a 26% higher UTS compared to the as-built state and a 3.6% higher UTS compared to the HT2 state (Figure 4). The HT1 state specimens exhibited the highest yield strength, with an 8.4% increase over the as-built state and 4.1% over the HT2 state. The investigation of the anisotropy revealed differences in tensile performance between directions: 17.4% for the as-built, 8.7% for the HT1, and 12.4% for the HT2 states. All states exhibited better tensile performance in the horizontal (X-axis) direction. The HT2 state showed no improvement in tensile properties over the HT1 state at room temperature. Compared to the manufacturer's heat-treated state (Table 3), both the HT1 and HT2 states exhibited worse tensile performance, averaging 13.5% and 16.7% lower tensile performance, respectively.

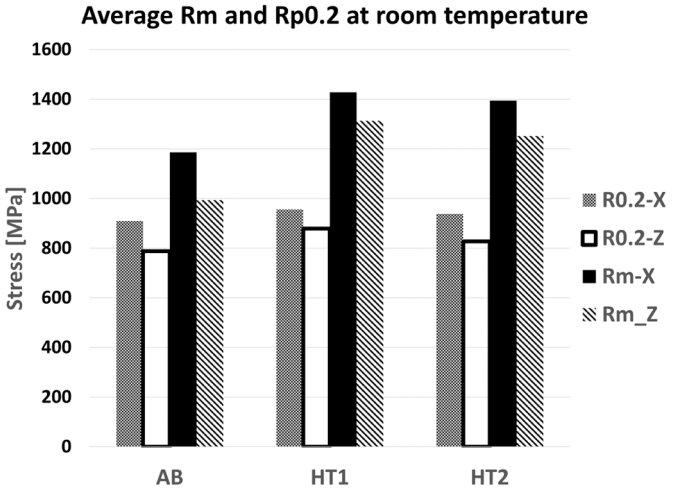


Figure 4. Inconel 939 Rm and Rp0.2 values for as-built, HT1, HT2 states at room temperature.

Table 3. Tensile tests yield strength and UTS values of as-built, HT1, and HT2 specimens at 23 degrees and 700 degrees Celsius with manufacturer's data [11].

	23 °C				700 °C			
	Yield Strength [MPa]		UTS [MPa]		Yield Strength [MPa]		UTS [MPa]	
	Horizontal	Vertical	Horizontal	Vertical	Horizontal	Vertical	Horizontal	Vertical
EOS as-built	880.0	740.0	1160.0	1090.0	-	-	-	-
As-built	909.3	788.3	1186.4	993.6	807.5	809.7	867.1	934.9
EOS heat-treated	1130.0	1100.0	1520.0	1500.0	860.0	910.0	1050.0	1050.0
HT1	956.7	879.7	1428.5	1313.0	680.5	791.3	681.5	970.9
HT2	938.9	827.8	1394.9	1251.9	672.5	754.3	678.1	817.4

At an elevated temperature of 700 °C, the specimens tested in the vertical (Z-axis) direction exhibited better tensile performance for all material states and parameters with the exception of yield strength for the as-built state (Figure 5). This behavior (contrary to the expectations for LPBF materials) aligns with the manufacturer's data [11] and findings by Hibino et al. (2022) [14]. The HT1 state exhibited worse tensile performance at an elevated temperature, with the exception of the UTS in the vertical (Z-axis) direction. The UTS in the vertical (Z-axis) direction for HT1 exhibited a 3.9% increase compared to the as-built state. The HT1 yield strength and UTS in the horizontal (X-axis) direction were 15.8% and 21.5% lower compared to the as-built state. The HT2 state experienced similar yield strength and UTS in the horizontal (X-axis) direction compared to the HT1 state. In the vertical (Z-axis) direction, the yield strength was 4.7%, and the UTS was 15.8% lower compared to the HT1 state. Relative to the manufacturer's data [11] (Table 3), in the heat-treated state, the HT1 state had 16% and 20% lower R0.2 and UTS, while the HT2 state had 17% and 29% lower R0.2 and UTS. The as-built state at an elevated temperature exhibited a 35% increase in yield strength and a 7% increase in UTS compared to Zou et al. (2023) [15].

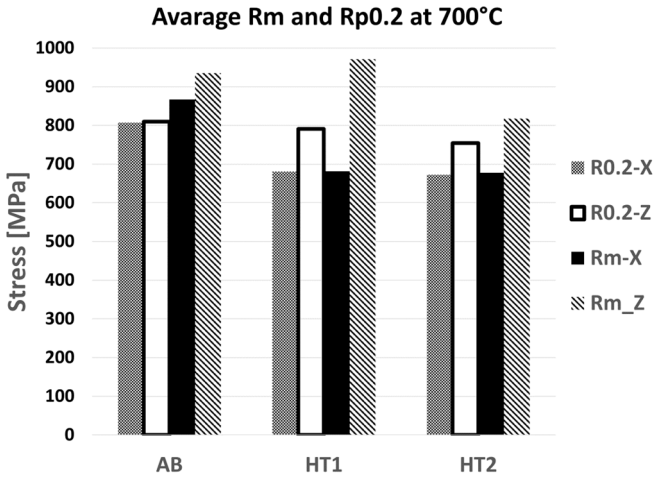


Figure 5. Inconel 939 Rm and Rp0.2 values for as-built, HT1, and HT2 states at elevated temperature.

3.2. Microstructure Analysis

The as-built state of the Inconel 939 alloy exhibits a typical nickel superalloy microstructure, featuring visible melt pools with dendritic structures growing across them. In the XY plane, melt pools are visible with a 67° rotation between layers (Figure 6A). In the XZ plane, the melt pools are uniform, indicating correct process parameters with no keyhole, under-melted, or balling melt pools, which confirms that the right parameters have been chosen (Figure 6B). The dendritic structures can be seen.

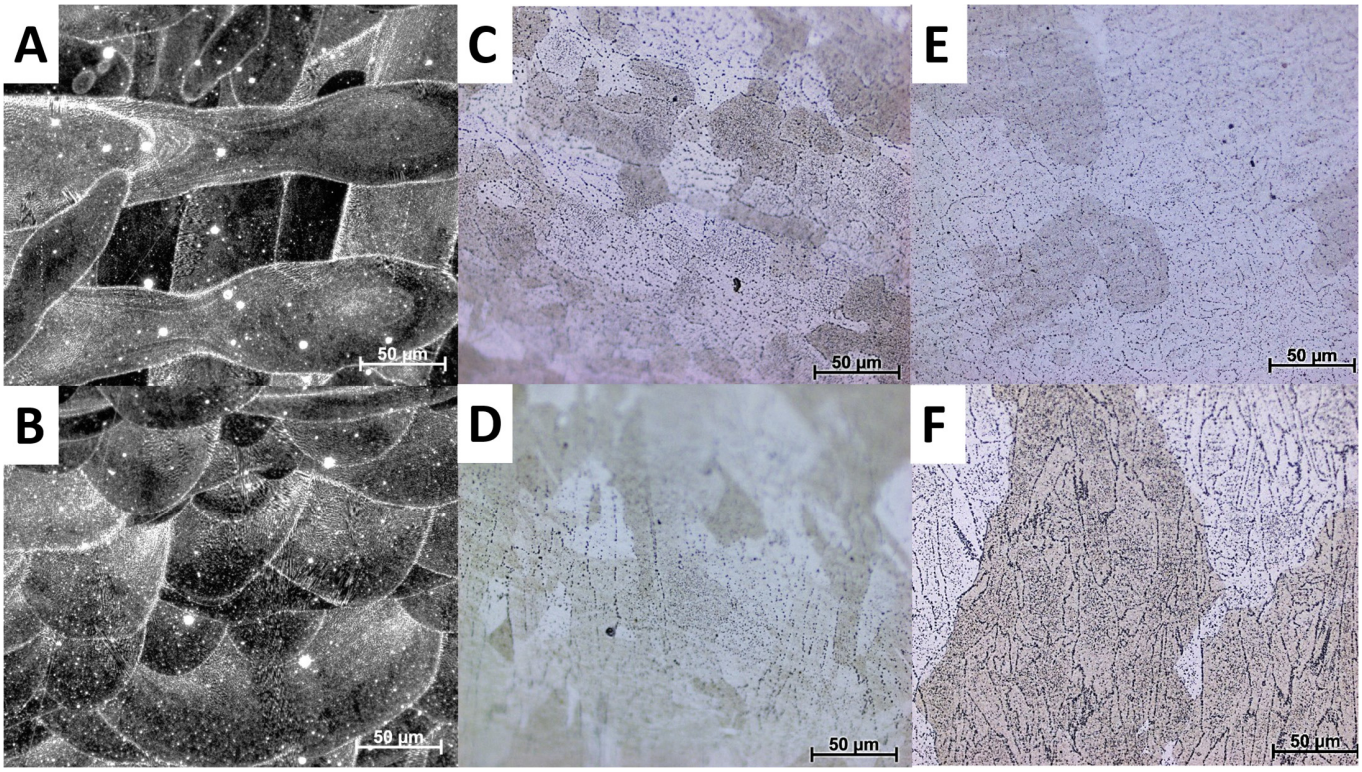


Figure 6. Microstructures of Inconel 939 in as-built (**A**,**B**), HT1 (**C**,**D**), and HT2 (**E**,**F**) states.

After the HT1 heat treatment, the microstructure shows elongated grains in the XZ plane and regular grains in the XY plane (Figure 6C,D), characteristic of LPBF nickel superalloys post-heat treatment. The dendritic structures are no longer visible. Black spots can be seen on the optical microscope, which have been identified using SEM as MC carbides, as they are rich in Nb, Ti, and Ta (Figure 7A–C), even though no increase in carbon has been measured. This can be due to the high mistake certainty of EDS in the case of oxygen and carbon. Hu et al. (2024) [16] also detected regions with high concentrations of Nb, Ti, and Ta, with no increase in carbon on EDS. They identified those regions as MC carbides using TEM; therefore, it can be assumed that in the case of Inconel 939, all EDS-detected regions with high concentrations of Nb, Ti, and Ta are MC carbides. Precipitates were observed both on grain boundaries and intragranularly. Light-gray γ′ precipitates were also visible (Figure 7B).

The HT2 heat treatment results in recrystallized grains, similar in size in both the XY and XZ planes (Figure 6E,F). The grains are more regular compared to the HT1 state but are highly elongated in the Z-axis. This can contribute to poorer tensile performance at elevated temperatures along the X-axis, as observed by Hibino et al. (2022) [14]. Larger grain areas in the X-axis facilitate dislocation movement, causing easier crack nucleation and propagation. The precipitates remain in similar positions as in the case of the HT1 state, but because of grain growth, a high amount of precipitates is present intragranularly. This is caused by the lack of movement of the carbide nuclei after the LPBF process, as explained by Philpott et al. (2016) [17] (Figure 7D–F). The precipitates were again identified as MC carbides, as they show high Nb, Ti, and Ta concentrations. γ′ precipitates appear as light-gray round spots.

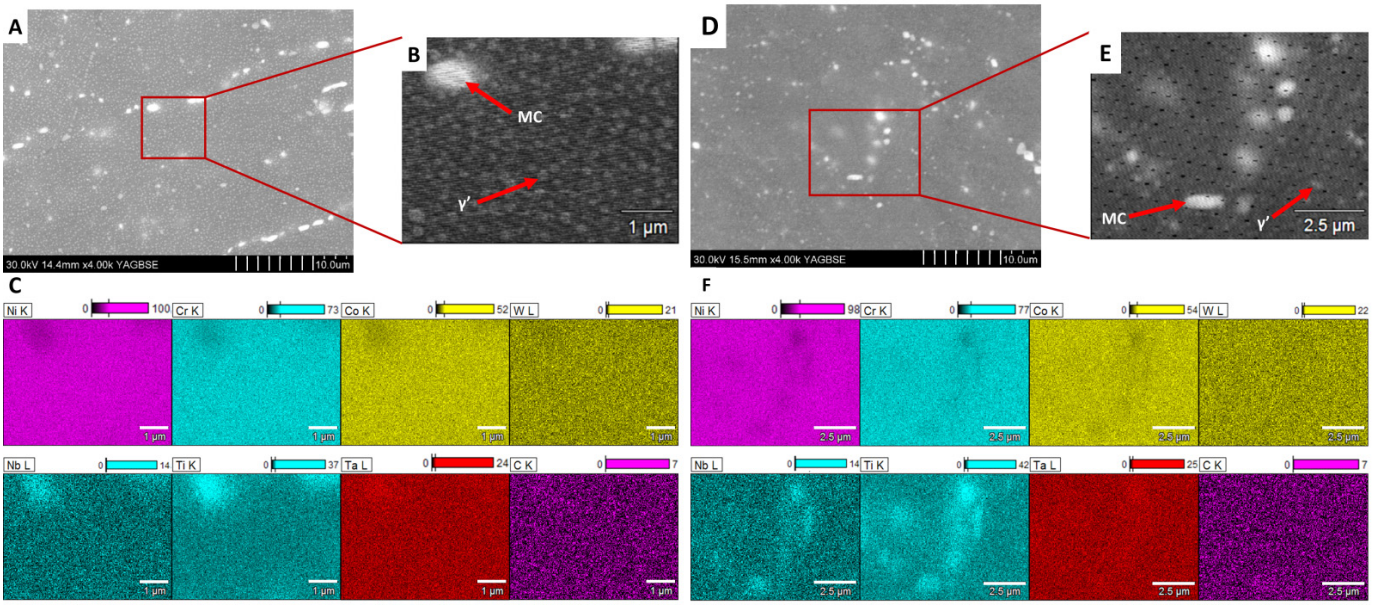


Figure 7. SEM micrograph of IN939 HT1 state YAGBSE detector (**A**); EDS-analyzed fragment (**B**); EDS maps of elements (**C**); HT2 state YAGBSE detector (**D**); EDS-analyzed fragment (**E**); EDS maps of elements (**F**).

The EBSD tests revealed that the as-built state of the Inconel 939 alloy contains numerous subgrains and deformed grains, which carry high amounts of energy from thermal stresses, causing distortions in LPBF-produced structures (Figure 8A,D; Table 4). The HT1 heat treatment did not cause recrystallization, and it consists primarily of subgrains with a reduced amount of deformed grains compared to the as-built state. A reduction in the number of deformed grains should provide an effective reduction in material stresses and distortions (Figure 8B,E; Table 4). The specimen after HT2 heat treatment has a microstructure with a high fraction of recrystallized grains. This suggests that the recrystallization process took place and deformations were eliminated (Figure 8C,F; Table 4). This confirms that the chosen solution treatment temperature produces a recrystallized microstructure. The lack of deformed grains should produce parts that are virtually free of distortion. Grain size varies, with the smallest grains (24.2 μm^2) after HT1 heat treatment and the largest (134.9 μm^2) after HT2 heat treatment (Table 5). At room temperature, the main strengthening mechanism is connected to the density of dislocations and the amount of dislocation-blocking grain boundaries. With the elongated grains in the Z-axis, the amount of grain boundaries across the X-axis is much higher, causing an increase in tensile performance in the X-axis compared to the Z-axis. At elevated temperatures, the effect of grain boundaries changes, and it is easier for dislocations to move across high-density grains, explaining why a switch between the X- and Z-axis tensile performance can be observed. The effect of the grain size difference between HT1 and HT2 is reduced mainly because of the number of precipitations present in both states, which also block dislocation movement.

Table 4. Recrystallization volume fractions of Inconel 939 for as-built, HT1, and HT2 states (% vol.).

	Recrystallized	Substructured	Deformed
AB	3.2%	44.0%	52.8%
HT1	3.9%	79.0%	17.1%
HT2	59.6%	40.4%	-

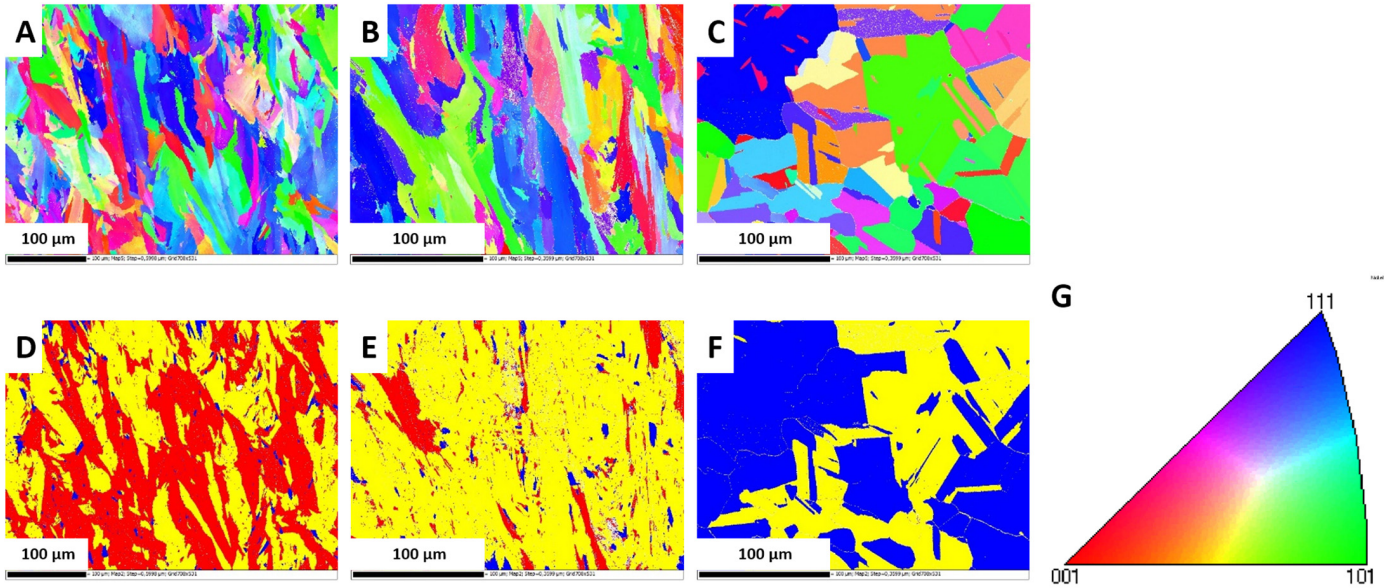


Figure 8. IPF (**A**–**C**) and recrystallization fraction (**D**–**F**) maps of Inconel 939 for as-built (**A**,**D**), HT1 (**B**,**E**), and HT2 (**C**,**F**) states; IPF color code for grain orientation (**G**).

Table 5. Average grain size of Inconel 939 for as-built, HT1, and HT2 states.

	Grain Size [µm^2]
AB	50.5
HT1	24.2
HT2	134.9

Hardness differences between HT1 and HT2 are negligible, indicating that precipitation has a more significant impact on hardness than grain size and recrystallization.

The heat-treated specimens experienced oxidation due to the use of a non-inert atmosphere furnace. On both the HT1 and HT2 states, three distinct layers were visible under the SEM microscope. A linear chemical analysis (Figure 9D,H) showed differences between each layer, and all of them were different from the initial alloy. The outermost layer contained a reduced amount of chromium with moderate amounts of nickel, titanium, and cobalt. This layer was present in small amounts on the HT1 state specimens. In the HT2 state specimens, it averaged 11.9 µm. The next layer showed increased amounts of chromium and titanium with limited nickel and cobalt (Figure 9C,G). This layer was present along the entire edge but varied in thickness, averaging 10.1 µm for HT1 and 11.5 µm for HT2; it could be identified as CrO_3 scales. The third layer contained numerous cracks. Both states had nominal amounts of nickel, tantalum, and cobalt with reduced amounts of chromium, while the cracks were titanium- and aluminum-rich. The thickness of this layer averaged 33.5 µm for the HT1 state and 44.8 µm for the HT2 state and could be identified as an internal oxidation zone (IOZ). Compared to Visibile et al. (2024) [18], we observed an additional layer on top of the CrO_3 scales, which may have been caused by the higher temperatures of our heat treatment compared to 900 degrees Celsius. This layer requires further investigation. The CrO_3 scales, in our case, consisted of a scarce amount of TiO, which had probably been transferred from the IOZ. Visibile et al. (2024) detected an additional layer—an internal nitridation zone (INZ)—no signs of which were present in our case, as titanium levels after the IOZ are nominal. It can be suspected that higher temperatures caused faster transfer of nickel, cobalt, and titanium through the CrO_3 scale layer, depleting the INZ from elements needed for the formation.

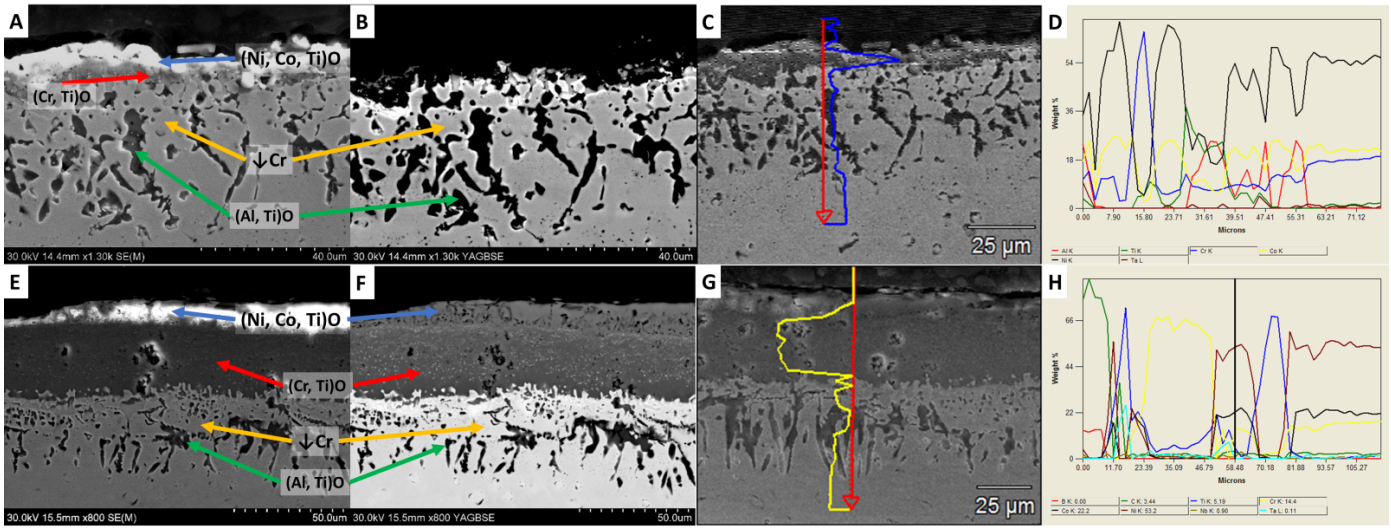


Figure 9. SEM micrographs of Inconel 939 oxidized edges for HT1 state SE detector (**A**); YAGBSE detector (**B**); EDS scanning line direction marked with red, with blue graph for weight% of Cr (**C**); EDS graph for marked line (**D**); HT2 state SE detector (**E**); YAGBSE detector (**F**); EDS scanning line direction marked with red, with yellow graph for weight% of Cr (**G**); EDS graph for marked line (**H**).

4. Conclusions

The investigation conducted in this study aimed to explore the influence of sub-recrystallization and recrystallization temperature during solution treatment on the mechanical performance of LPBF-produced Inconel 939 alloy. The verification of hypotheses provided valuable insights into the behavior of the alloy under varying thermal conditions and shed light on the critical aspects influencing its mechanical properties.

- Impact of Solution Treatment Temperature on Carbide Redistribution:

The analysis confirmed that higher solution treatment temperatures significantly impact carbide redistribution within LPBF-produced Inconel 939 parts. A microstructural examination revealed distinct changes in grain structure and precipitation distribution, particularly the migration of carbides from grain boundaries to intragranular regions. This finding underscores the importance of precise control over heat treatment parameters to achieve the desired microstructural evolution.

- Effect of Solution Treatment Temperature on Mechanical Performance:

Contrary to initial expectations, this study found that an increase in solution treatment temperature does not necessarily lead to improved mechanical performance for LPBF-produced Inconel 939 parts. Tensile tests revealed that higher heat treatment temperatures resulted in inferior mechanical properties, particularly in terms of tensile strength at room temperature. The formation of larger recrystallized grains with intragranular carbides in the HT2 state contributed to this decline in mechanical performance.

- Prerequisites for Optimal Mechanical Behavior:

This research underscores the importance of precise control over heat treatment parameters to achieve optimal mechanical behavior in LPBF-produced Inconel 939 components. It highlights the need for a comprehensive understanding of the interplay between alloy composition, initial microstructure, and specific heat treatment conditions. This knowledge is essential for guiding future efforts aimed at enhancing the mechanical performance of the alloy.

- Recommendations for Further Studies:

Building upon the insights gained from this study, several recommendations for further research are proposed. These include investigating alloy modifications using

elements such as Re and ODS to improve high-temperature performance and optimizing solution treatment times with aging parameters to enhance tensile performance.

Author Contributions: Conceptualization, P.P. and J.M.; Methodology, P.P., D.M. and J.M.; Software, P.P.; Formal analysis, P.P., D.M. and J.M.; Investigation, P.P., D.M., K.P. and M.W.-C.; Data curation, P.P. and D.M.; Writing—original draft, P.P.; Writing—review & editing, D.M., K.P. and J.M.; Visualization, P.P.; Supervision, J.M.; Project administration, J.M.; Funding acquisition, J.M. All authors have read and agreed to the published version of the manuscript.

Funding: This research was funded by Faculty of Materials Science and Engineering, Warsaw University of Technology's subsidy "Materials for working in extreme conditions"—2023.

Institutional Review Board Statement: Not applicable.

Informed Consent Statement: Not applicable.

Data Availability Statement: All data included in this study are available upon request by contact with the corresponding author.

Conflicts of Interest: The authors declare no conflicts of interest.

References

1. ESA-ASPIRER: Aerospike Rocket Engine with 6000 Newton Thrust from the Powder Bed 3D Printer. Fraunhofer Institute for Material and Beam Technology IWS. Available online: https://www.iws.fraunhofer.de/en/newsandmedia/news/2022-03-22_news_esa-aspirer.html (accessed on 25 September 2023).
2. Aerosint—Multi-Material 3D Printing. Available online: https://aerosint.com/ (accessed on 29 August 2023).
3. AI Steps into Space with Part Design and Smart Exploration. Available online: https://www.designnews.com/design-software/ai-steps-space-part-design-and-smart-exploration (accessed on 29 August 2023).
4. McCann, R.; Obeidi, M.A.; Hughes, C.; McCarthy, É.; Egan, D.S.; Vijayaraghavan, R.K.; Joshi, A.M.; Garzon, V.A.; Dowling, D.P.; McNally, P.J.; et al. In-situ sensing, process monitoring and machine control in Laser Powder Bed Fusion: A review. *Addit. Manuf.* **2021**, *45*, 102058. [CrossRef]
5. Everton, S.K.; Hirsch, M.; Stravroulakis, P.; Leach, R.K.; Clare, A.T. Review of in-situ process monitoring and in-situ metrology for metal additive manufacturing. *Mater. Des.* **2016**, *95*, 431–445. [CrossRef]
6. Shaikh, A.S.; Rashidi, M.; Minet-Lallemand, K.; Hryha, E. On as-built microstructure and necessity of solution treatment in additively manufactured Inconel 939. *Powder Metall.* **2023**, *66*, 3–11. [CrossRef]
7. Shaikh, A.S. Development of a γ′ Precipitation Hardening Ni-Base Superalloy for Additive Manufacturing. Master's Thesis, Chalmers University of Technology, Gothenburg, Sweden, 2018. [CrossRef]
8. Gibbons, T.B.; Stickler, R. IN939: Metallurgy, Properties and Performance. In *High Temperature Alloys for Gas Turbines 1982*; Brunetaud, R., Coutsouradis, D., Gibbons, T.B., Lindblom, Y., Meadowcroft, D.B., Stickler, R., Eds.; Springer: Dordrecht, The Netherlands, 1982; pp. 369–393. [CrossRef]
9. Formenti, A.; Eliasson, A.; Mitchell, A.; Fredriksson, H. Solidification sequence and carbide precipitation in Ni-base superalloys IN718, IN625 AND IN939. *High Temp. Mater. Process.* **2011**, *24*, 239–258. [CrossRef]
10. Banoth, S.; Li, C.W.; Hiratsuka, Y.; Kakehi, K. The effect of recrystallization on creep properties of alloy in939 fabricated by selective laser melting process. *Metals* **2020**, *10*, 1016. [CrossRef]
11. "EOS NickelAlloy IN939", EU—EOS Store. Available online: https://www.eos.info/05-datasheet-images/Assets_MDS_Metal/EOS_NickelAlloy_IN939/Material_DataSheet_EOS_NickelAlloy_IN939_en.pdf (accessed on 24 September 2023).
12. Molak, R.M.; Paradowski, K.; Brynk, T.; Ciupinski, L.; Pakiela, Z.; Kurzydlowski, K.J. Measurement of mechanical properties in a 316L stainless steel welded joint. *Int. J. Press. Vessel. Pip.* **2009**, *86*, 43–47. [CrossRef]
13. Molak, R. Zastosowanie Minipróbek do Wyznaczania Właściwości Mechanicznych. Ph.D. Thesis, Warsaw University of Technology, Warsaw, Poland, 2011.
14. Hibino, S.; Fujimitsu, K.; Azuma, M.; Ishimoto, T.; Nakano, T. Effects of Recrystallization on Tensile Anisotropic Properties for IN738LC Fabricated by Laser Powder Bed Fusion. *Crystals* **2022**, *12*, 842. [CrossRef]
15. Zou, T.; Liu, M.; Cai, Y.; Wang, Q.; Jiang, Y.; Wang, Y.; Gao, Z.; Pei, Y.; Zhang, H.; Liu, Y.; et al. Effect of temperature on tensile behavior, fracture morphology, and deformation mechanisms of Nickel-based additive manufacturing 939 superalloy. *J. Alloys Compd.* **2023**, *959*, 170559. [CrossRef]
16. Hu, P.; Liu, Z.; Zhang, H.; Li, Y.; Zhou, Q.; Xie, J. Effect of remelting on cracking of Inconel 939 fabricated via laser powder bed fusion. *Mater. Charact.* **2024**, *214*, 114087. [CrossRef]

17. Philpott, W.; Jepson, M.; Thomson, R. Comparison of the Effects of a Conventional Heat Treatment Between Cast and Selective Laser Melted IN939 Alloy. 2016. Available online: https://repository.lboro.ac.uk/articles/conference_contribution/Comparison_of_the_effects_of_a_conventional_heat_treatment_between_cast_and_selective_laser_melted_IN939_alloy/9233600/1 (accessed on 23 November 2023).
18. Visibile, A.; Gunduz, K.O.; Sattari, M.; Fedorova, I.; Halvarsson, M.; Froitzheim, J. High temperature oxidation of inconel 939 produced by additive manufacturing. *Corros. Sci.* **2024**, *233*, 112067. [CrossRef]

Disclaimer/Publisher's Note: The statements, opinions and data contained in all publications are solely those of the individual author(s) and contributor(s) and not of MDPI and/or the editor(s). MDPI and/or the editor(s) disclaim responsibility for any injury to people or property resulting from any ideas, methods, instructions or products referred to in the content.